Compressive response of a 3D non-woven carbon-fibre composite

S. Das[a], K. Kandan[a,b], S. Kazemahvazi[a], H.N.G. Wadley[c] and V.S. Deshpande[a*]

[a] *Department of Engineering, University of Cambridge, Trumpington Street, Cambridge CB2 1PZ, UK.*

[b] *School of Engineering, De Montfort University, The Gateway, Leicester LE1 9BH, UK.*

[c] *Department of Material Science & Engineering, School of Engineering and Applied Science, University of Virginia, Charlottesville, VA 22904, USA.*

Abstract

The compressive response of a three-dimensional (3D) non-interlaced composite comprising three orthogonal sets of carbon fibre tows within an epoxy matrix is analysed. First, the compressive response is measured in three orthogonal directions and the deformation/failure modes analysed by a combination of X-ray tomography and optical microscopy. In contrast to traditional unidirectional and two-dimensional (2D) composites, stable and multiple kinks (some of which zig-zag) form in the tows that are aligned with the compression direction. This results in an overall composite compressive ductility of about 10% for compression in the low fibre volume fraction direction. While the stress for the formation of the first kink is well predicted by a usual micro-buckling analysis, the composite displays a subsequent hardening response associated with formation of multiple kinks. Finite element (FE) calculations are also reported to analyse the compressive response with the individual tows modelled as anisotropic continua via a Hill plasticity model. The FE calculations are in good agreement with the measurements including prediction of multiple kinks that reflect from the surfaces of the tows. The FE calculations demonstrate that the three-dimensionality of the microstructure constrains the kinks and this results in the stable compressive response. In fact, the hardening and peak strength of these composites is not set by the tows in direction of compression, but rather set by the out-of-plane compressive response of the tows perpendicular to the compression direction.

*Corresponding author. E-mail address: vsd@eng.cam.ac.uk.

1. Introduction

Carbon fibre reinforced polymer (CFRP) composites are widely utilized in aerospace and automotive structures due to their high strength and stiffness to weight ratios (Poe et al., 1999; Stig, 2012). These long fibre composites are designed to possess high axial stiffness and tensile strength but the compressive strength of unidirectional composites rarely exceeds 60% of their tensile strength. The main competing mechanisms governing the compressive strength of long fibre composites are: (i) elastic micro-buckling (an elastic instability involving matrix shear); (ii) plastic micro-buckling in which the matrix deforms plastically; (iii) fibre crushing (a compressive fibre failure mode); (iv) splitting by matrix cracking parallel to the main fibre direction; (v) buckle delamination and (vi) shear band formation at 45^{o} to the main axis of loading due to matrix yielding (Fleck, 1997).

In composites with high toughness matrices, the micro-buckling and fibre crushing modes are most commonly encountered. For example, the compressive strength of glass and carbon fibre polymer reinforced composites (GFRP and CFRP, respectively) is usually governed by elastic or plastic micro-buckling. While the micro-buckling strength is typically set by matrix properties, Kyriakides and Ruff (1997) showed that the wavelength, amplitude, distribution of imperfections and fibre waviness also strongly influence the strength of long-fibre composites. Moreover, Vogler and Kyriakides (1997) demonstrated that CFRP and GFRP composites could continue to carry (a reduced) load after the onset of micro-buckling by the broadening of the kink band. However, the compressive ductility (defined as the compressive strain at which the material has a significant loss in load carrying capacity) of traditional CFRPs (unidirectional or two-dimensional (2D) composites comprising laminated or woven layers) is about 2% to 4%. Competing lightweight metallic materials such as Aluminium and Magnesium have a significantly higher compressive resilience with nearly no loss in compressive load carrying capacity after initial yield. This limits the application of CFRPs in situations that for example require maintenance of structural integrity after impact loading.

There exists a large literature on theoretical/numerical studies with the aim of improving the understanding of constituent properties of the composite that set the compressive ductility. For example, Laffan et al. (2012) investigated the compressive

toughness and strength of notched unidirectional (UD) carbon fibre composites. Unlike Sivashankar et al. (1996), they observed that calculations based on an effective compressive stress intensity factor (this is defined using the understanding the fields at the tip of a kink-band are similar to that ahead of a crack) were unable to predict the measurements with sufficient fidelity and attributed this discrepancy to failure modes such as crushing, band broadening and delamination that were not appropriately accounted for in the toughness model. Finite element (FE) calculations also reported by Laffan et al. (2012) reproduced these mechanisms with sufficient fidelity so that predictions of failure stresses had a high level of accuracy. These findings were further reinforced by Pinho et al. (2012) who emphasized the role of matrix splitting in governing the micro-buckling stresses and Wind et al. (2015) who showed that a FE model in which the fibres and matrix were explicitly modelled accurately captured the 4-point bend response of a notched CFRP specimen.

Since matrix cracking is an important mechanism that results in the loss of compressive ductility, the tailoring of fibre/tow architectures in CFRPs has been widely used to improve the compressive response. The most common approaches include modifying 2D composites by adding out-of-plane reinforcements. This is typically achieved by Z-pinning (Freitas et al., 1994; Mouritz, 2007), stitching (George et al., 2014; Malcom et al., 2013) and knitting (Kamiya et al., 2000). In addition, a range of techniques has been developed to manufacture three-dimensional (3D) fabrics wherein tows are present in at-least three orthogonal directions; see Khokar (2002) for a detailed review of these techniques. In brief, 3D fabrics fall into three categories: (i) 2D woven 3D fabrics produced by usual 2D weaving methods with mono-directional shedding[1]; (ii) 3D woven 3D fabrics produced by a dual-direction shedding system and (iii) non-woven 3D fabrics without interlacing or interweaving produced by a technique known as “noobing” that is described in Section 2. The ability to manipulate the volume fractions of fibre in three directions not only allows tailoring of the multi-axial properties of composites (Quinn et al., 2008); it also reduces the susceptibility to delamination, which results in an improvement in the impact performance of CFRPs (McIlhagger et al., 2007, 2008;

[1] In weaving *shed* is the channel created for passing weft by temporarily cross-separating the warp yarns to achieve interlacing between the warps and wefts. The term *shedding* refers to the action of creating a shed.

Tan et al., 2000). Moreover 3D composites can add more functionality to any eventual component as discussed by Stig (2012).

Most 3D woven composites suffer from a relatively low modulus due to significant fibre crimp or waviness. In an attempt to overcome this drawback, Kuo and Ko (2000) modified a conventional weaving machine to produce 3D fabrics with orthogonal, non-interlacing yarns. They demonstrated that such a composite had a high compressive ductility due to the confinement imposed by the off-axis yarns. In a subsequent study, Kuo et al. (2007) demonstrated the formation of multiple kinks within the tows of such 3D composites. However, the inherent limitations of their modified weaving process resulted in high fibre waviness and hence reduced compressive strengths in the composites they investigated. Moreover, no detailed theoretical/numerical investigations have been reported to-date to understand the compressive failure mechanisms in such composites.

The main focus of this study is to develop an understanding of the compressive failure mechanisms in 3D non-woven carbon fibre/epoxy composites manufactured by the noobing process. This process significantly reduces fibre waviness and hence has the potential to significantly enhance the compressive strength of such composites. The outline of the study is as follows. We first briefly describe the manufacturing process and the microstructure of these 3D composites. Next, we report the compressive failure response along with detailed imaging to illustrate the deformation/failure modes. Finally, we report FE calculations of the compressive responses with the individual tows modelled as anisotropic continua.

2. Materials, manufacture and property estimates

The principle of 3D fabric forming/manufacture by the noobing process is fundamentally different from traditional weaving, knitting or braiding processes. In brief, linear sets of yarns in either “uniaxial” or “multi-axial” arrays (see Fig. 1 for definitions of uniaxial and multi-axial) are bound/tied together by another set of yarns to produce a 3D layerless fabric. Since the yarns do not interlace, interloop or intertwine the fabrics are referred to as *noobed* (the acronym NOOB standing for Non-interlacing, Orientating Orthogonally and Binding) fabrics (Khokar, 1996).

There are a variety of noobing processes and readers are referred to Khokar (2002) for a detailed discussion. Here we briefly describe the process used to manufacture the noobed materials used in this study.

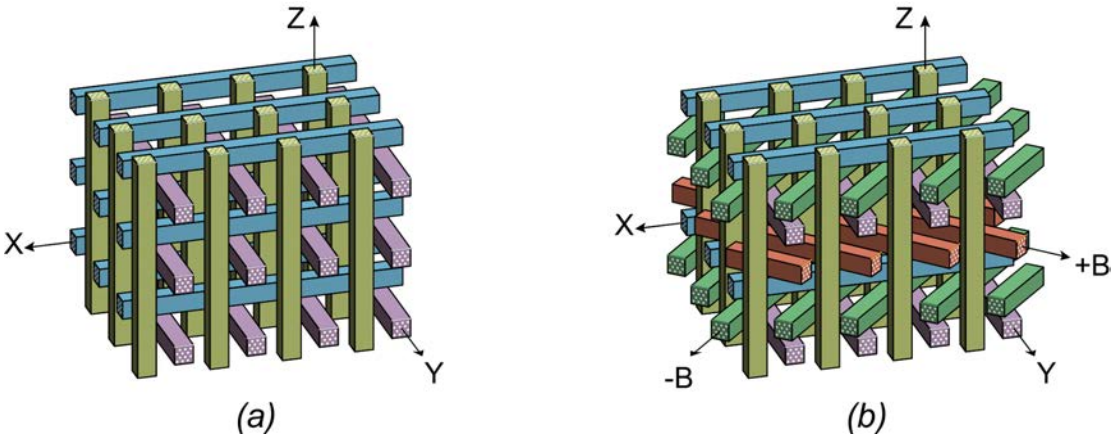

Figure 1: Sketches of the two types of non-woven 3D fabrics: (a) "uniaxial" fabrics comprising orthogonal yarns in the X, Y and Z-directions and (b) "multi-axial" fabrics with 5 yarn directions ($\pm B$ in addition of the X, Y and Z-direction yarns).

2.1 The noobing process and composite manufacture

The composites were manufactured in two steps: first the dry 3D fabrics were produced in block form and then infused with the epoxy matrix. The 3D fabrics were manufactured[2] using the method developed by Khokar (2012) that we briefly describe here. With (X, Y, Z) forming a Cartesian co-ordinate system, the composite comprises an array of Z-yarns bound together by X and Y-yarns that traverse the rows and columns of the grid formed by the Z-yarns. These X and Y-yarns loop as shown in Fig. 2a and bind the fabric together. Readers are referred to Khokar (2012) for details of the device used for the automated manufacture of this 3D fabric. We emphasize here that this fabric is produced by a process that does not involve shedding as in a weaving process and comprises three orthogonal non-interlaced X, Y and Z-yarns. The noobed fabric is relatively stable as it is well bound together on all sides by the looping X, Y and Z yarns (in Fig. 2a, looping by only X and Y yarns are shown for the sake of clarity). Infusion of a polymer matrix is performed via a resin transfer moulding process (RTM) to produce the 3D composite material.

[2] The noobed fabrics were supplied by Biteam AB, Danderydsgatan 23, SE-114 26 Stockholm, Sweden but are now available from Fureho AB, Segloravägen 6, SE-504 64 Borås, Sweden.

2.2 Material geometry

The 3D noobed composites used here comprise Toray T700S 12k carbon fibre tows (non-twisted carbon fibre yarns are usually referred to as tows) in a NM FW3070 epoxy matrix[3] with a glass transition temperature of 180^{o}C. The carbon fibres in the 12k tows are approximately $d = 7.2$ μm in diameter and the 3D composite was anisotropic with 20% of the total number of tows in Z-direction and 40% each in the X and Y-directions. Blocks of the 3D noobed composites of size $175\ (X)$mm $\times$ $103\ (Y)$mm $\times 45\ (Z)$mm were manufactured and specimens of required dimensions were cut from these blocks using a diamond band saw.

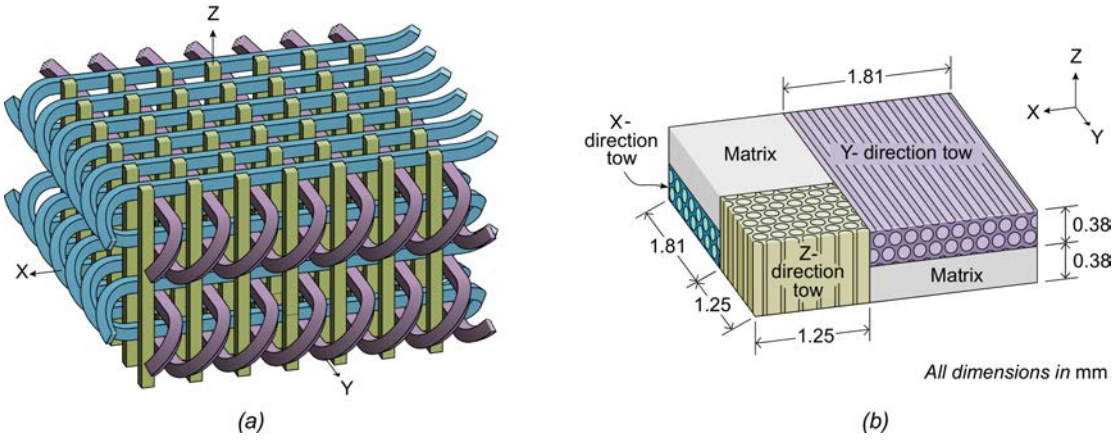

Figure 2: (a) Sketch of the orthogonal non-woven yarns in the 3D noobed fabric that is infused to give the composite. The X and Y-yarns form closed loops that bind together the 3D fabric. (b) Sketch of the unit cell of the 3D noobed composite employed in this study. The unit cell is inferred from the XCT images in Fig. 3.

In order to evaluate the micro-structure of the as-produced (noobed + infused) composites, square specimens of side roughly 20 mm were cut from the block and imaged via X-ray computed tomography (XCT). The XCT images of the interior of the specimens on three orthogonal planes are shown in Fig. 3. The specimen was cut from the edge of the block so as to also visualise the looped tows (Fig. 2a). These images clearly show that while the Z-direction tows have an approximately square cross-section the X and Y-direction tows are flattened in the Z-direction during the

[3] Nils Malmgren AB, P.O.Box 2039 S-442 02 Ytterby Sweden.

RTM process. Moreover, the geometry of the orthogonal arrangement of the tows requires that pockets of pure matrix (in addition to the matrix that exists between fibres within each tow) are regularly interspersed in the composite. The periodic unit cell as inferred from these XCT images is sketched in Fig. 2b (an average unit cell based on measurements at 30 different locations in the XCT images) and includes all the relevant dimensions of the tows and matrix pockets.

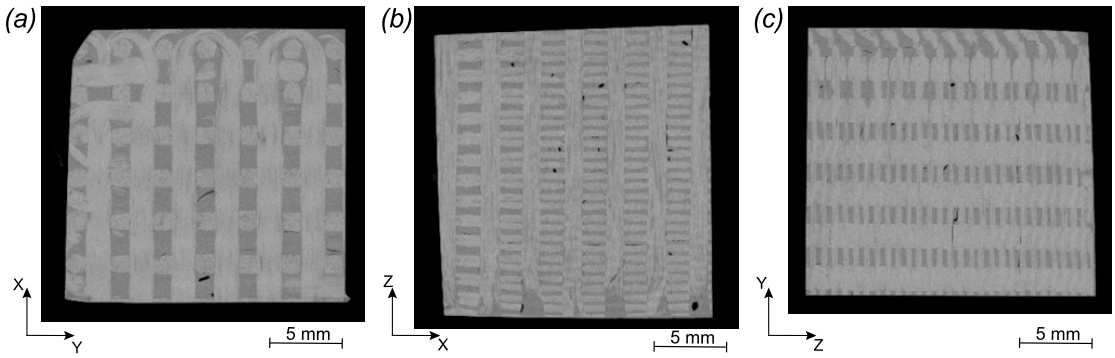

Figure 3: X-ray tomographic (XCT) scans of the 3D noobed composite showing sections on three orthogonal planes. The (X, Y, Z) co-ordinate system is based on the noobing process where the X and Y-yarns form a closed loop (Fig. 2a).

2.2.1 Volume fractions

The composite comprises four principal phases: (i) the X, Y and Z-direction tows and (ii) matrix pockets. Based on the unit cell with dimensions sketched in Fig. 2b, the X and Y-direction tows comprise a volume fraction $v_X = v_Y \approx 29\%$ of the composite while the Z-direction tows occupy a volume fraction $v_Z \approx 17\%$ of the composite. The remainder $v_M = 25\%$ of the volume is occupied by the matrix pockets. It now remains to specify the overall carbon fibre volume fraction within the composite. Recall that each tow comprises 12k fibres of diameter 7.2 μm. Then based on the tow cross-sectional areas from Fig. 2b the fibre volume fractions in the X and Y-direction tows are $f_X = f_Y \approx 68\%$ while the Z-direction tow comprises $f_Z \approx 30\%$ fibres. The overall fibre volume fraction in the composite then follows as $f = 2v_X f_X + v_Z f_Z \approx 45\%$. The area fractions of the different phases are also of interest in the subsequent derivations of material properties. We calculate these area fractions on the surfaces of the cuboidal unit cell sketched in Fig. 2b. For example, the area fraction of the Z-direction tows on the $X - Y$ plane is denoted as $\bar{A}^Z_{XY}$: the dimensions given in Fig. 2b

specify that $\bar{A}_{XY}^{Z} = 0.17$. For brevity, we do not state here all such possible area fractions that can be readily calculated from the dimensions in Fig. 2b.

2.3 Material properties

The 3D noobed composite comprised Toray T700S 12k carbon fibre tows in a NM FW3070 epoxy matrix. The properties of these two constituents as given by the fibre and matrix manufacturers are:

(i) The fibre Young's modulus and Poisson's ratio are $E_f = 210$ GPa and $\nu_f = 0.25$, respectively while the tensile strength of the fibres, $\sigma_f = 4$ GPa.

(ii) The matrix Young's modulus and Poisson's ratio are $E_m = 3$ GPa and $\nu_m = 0.25$, respectively while the matrix tensile yield strength, $\sigma_m = 140$ MPa.

These properties of the constituents can be used to derive estimates of the effective properties of the different phases in the 3D noobed composite comprised of four phases. The Z-direction tows have a significantly larger cross-sectional area compared to the X and Y-direction tows. Thus, for purposes of the approximate analysis presented in Section 3 and the detailed finite element (FE) calculations in Section 4 we shall explicitly consider the Z-direction tows but model the X and Y-direction tows and the matrix pockets that surround the Z-direction tows as a single *effective medium*. We shall thus first derive effective properties for the tows and then use them to estimate properties of this effective medium. For the sake of brevity, we shall subsequently refer to this effective medium as a *homogenised matrix*. All the relevant anisotropic properties will be stated using the global co-ordinate system. For example, E_Z^Z and E_X^Z denote the longitudinal and transverse moduli, respectively of the Z-direction tow (the superscript specifies that these properties relate to the Z-direction tow while the subscripts specify the direction of the property). Similarly, E_X^X and E_Z^X are the longitudinal and transverse moduli, respectively of the X-direction tow while E_X^h and E_Z^h are the moduli of the homogenised matrix in the X and Z-directions, respectively.

2.3.1 Elastic properties

The tows are assumed to be transversely isotropic with the fibre direction normal to the plane of isotropy. We first consider the Z-direction tows. The longitudinal

modulus E_Z^Z is given by the Voigt bound as $E_Z^Z = f_Z E_f + (1 - f_Z)E_m$ while the transverse moduli $E_X^Z = E_Y^Z$ are given by the equivalent Reuss bound. Since the Poisson's ratios of the matrix and fibres are assumed equal, we take $\nu_{ZX}^Z = \nu_{XY}^Z = \nu_m$ and the shear modulus G_{XZ}^Z is estimated from a Reuss bound such that

$$\frac{1}{G_{XZ}^Z} = \frac{2(1+\nu_f)f_Z}{E_f} + \frac{2(1+\nu_m)(1-f_Z)}{E_m}. \qquad (2.1)$$

The five independent elastic constants required to describe the elastic properties of the transversely isotropic Z-direction tows are listed in Table 1. Equivalent estimates can be evaluated for the X (or Y)-direction tows with f_Z replaced by f_X. These properties are also listed in Table 1 for the X-direction tow. Note that the X-direction is normal to the plane of isotropy for the X-direction tow and hence the components of the elasticity tensor listed in Table 1 differ for the X and Z-direction tows.

We proceed to calculate the properties of the homogenised matrix that surrounds the Z-direction tows. From the unit cell sketched in Fig. 2b it is clear that this homogenised matrix is an orthotropic effective material with Young's moduli equal in the X and Y-directions. Thus, in order to simplify the constitutive description it is reasonable to assume that this homogenised matrix is also transversely isotropic with the Z-direction being normal to the plane of isotropy. Again, since all the constituents have equal Poisson's ratios it is reasonable to take $\nu_{ZX}^h = \nu_{XY}^h = \nu_m$. The Voigt estimate for the moduli $E_X^h = E_Y^h$ is given as

$$E_X^h = \frac{v_X(E_X^X + E_Y^X) + v_m E_m}{2v_X + v_m}, \qquad (2.2)$$

while that for modulus E_Z^h is

$$E_Z^h = \frac{2v_X E_Y^X + v_m E_m}{2v_X + v_m}. \qquad (2.3)$$

Similarly, the shear modulus G_{XZ}^h is given by the Voigt bound as

$$G_{XZ}^h = \frac{v_X(G_{YZ}^X + G_{XZ}^X) + v_m \dfrac{E_m}{2(1+\nu_m)}}{2v_X + v_m}, \qquad (2.4)$$

where $G_{YZ}^X = 0.5E_Y^X/(1+\nu_{ZY}^X)$. The five independent elastic constants for this effective medium are listed in Table 1.

Z-direction tow	$E_Z^Z = 65$	$E_X^Z = E_Y^Z = 4.2$	$\nu_{ZX}^Z = 0.25$	$\nu_{XY}^Z = 0.25$	$G_{XZ}^Z = G_{YZ}^Z = 1.7$
X-direction tow	$E_Z^X = E_Y^X = 8.8$	$E_X^X = 142$	$\nu_{XZ}^X = 0.25$	$\nu_{ZY}^X = 0.25$	$G_{XZ}^X = G_{XY}^X = 3.6$
homogenised matrix	$E_Z^h = 7.1$	$E_X^h = E_Y^h = 54$	$\nu_{ZX}^h = 0.25$	$\nu_{XY}^h = 0.25$	$G_{XZ}^h = G_{YZ}^h = 2.8$

Table 1: The elastic properties of the transversely isotropic tows and the homogenised matrix in the 3D noobed composite. The X and Y -direction tows have identical properties with the super/subscript X replaced by Y. All the moduli are given in GPa.

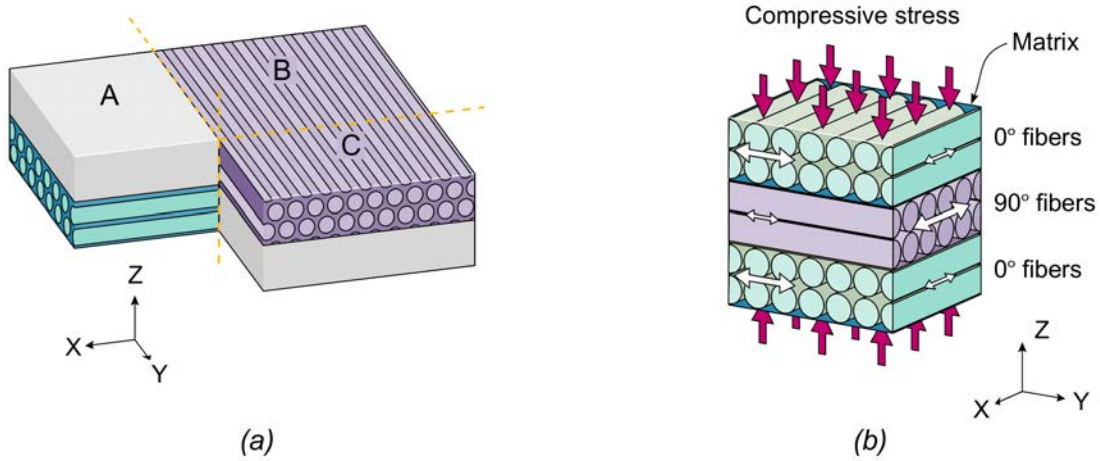

Figure 4: (a) Sketch of the homogenised matrix within the unit cell with the constituents of the homogenised matrix also indicated. The three regions A, B and C into which the homogenised matrix within the unit cell is divided for the analysis of the effective properties are also indicated. (b) Sketch of the indirect tension mechanism operative during the compression of region B in the Z-direction.

2.3.2 Plastic/failure strengths

In estimating the plastic/failure strengths of the different phases we note that the strength for tensile loading along the fibre direction is limited by the failure strength σ_f of the fibres while loading in other directions (e.g. transverse or shear loading) is

limited by flow of the matrix around fibres. Since the fibre strength is significantly greater than the matrix strength, the fibres may be assumed to be rigid for the purposes of analysis of strength in matrix flow governed regimes. With this understanding we proceed to develop estimates for the anisotropic strengths of the tows and the homogenised matrix.

First consider the Z-direction tow. The longitudinal tensile strength is limited by fibre fracture and directly given by a Voigt estimate as $Y_Z^Z = f_Z\sigma_f + (1 - f_Z)\sigma_m$. The calculation of the transverse strength is more complex. A Reuss estimate assuming rigid fibres will specify that the transverse strength is equal to that of the matrix. However, this is a poor estimate as the rigid fibres constrain the flow of the matrix and enhance the strength. Bele and Deshpande (2015) provided a simple analytical estimate (verified via FE calculations) for the transverse strength of a composite comprising rigid cylinders dispersed in a plastic matrix. Here we use that prescription to estimate the transverse and shear strengths of the tow. The Hashin lower bound (Hashin, 1962) for the Young's modulus E of a composite comprising a volume fraction f_Z of rigid inclusions in an incompressible matrix of modulus E_m is

$$\frac{E}{E_m} = 1 + \frac{5f_Z}{2(1 - f_Z)}. \qquad (2.5)$$

This linear bound can be transformed to an estimate of the strength using the method proposed by Suquet (1993) in which Eq. (2.5) is employed as a fictitious linear comparison composite. The transverse strength is then given as

$$Y_X^Z = Y_Y^Z = \sigma_m \sqrt{\frac{E}{E_m}(1 - f_Z)}, \qquad (2.6)$$

with E/E_m given by Eq. (2.5). The shear strengths are assumed to be related to the transverse strength via a Tresca yield criterion such that $Y_{XY}^Z = Y_{XZ}^Z = Y_{ZY}^Z = Y_X^Z/2$. These properties of the Z-direction tow are listed in Table 2. The plastic/failures strengths for the X-direction tow can also be estimated in an analogous manner and these predictions are also listed in Table 2.

Next consider the homogenised matrix sketched in Fig. 4a. Uniaxial loading in the X-direction results in longitudinal and transverse loading of the X-direction and Y-

direction tows, respectively as well as loading of the matrix pockets. The average stress sustained by this homogenised material at failure then follows as

$$Y_X^h = \bar{A}_{ZY}^X (Y_X^X + \sigma_m) + 0.5\bar{A}_{ZY}^Z (\sigma_m + Y_Y^X), \qquad (2.7)$$

with $Y_Y^h = Y_X^h$. In order to calculate the strength Y_Z^h it is convenient to divide the $X-Y$ plane of the homogenised matrix into three regions A, B and C as shown in Fig. 4a. The uniaxial stress in the Z-direction over regions A and C is limited to the matrix yield strength σ_m while compression of region B is equivalent to the compression of a cross-ply laminate. The out-of-plane compression of a cross-ply laminate results in the development of tensile stresses in the fibres due to the anisotropic Poisson expansion of the cross-plies (Fig. 4b). This so-called indirect tension mechanism was analysed by Attwood et al. (2014) who showed that the compressive strength of cross-ply laminates equals the in-plane tensile strength Y_X^X of each lamina. The strength Y_Z^h then is given by the average over the three regions such that

$$Y_Z^h = \frac{2\bar{A}_{XY}^m \sigma_m + (1 - \bar{A}_{XY}^Z - 2\bar{A}_{XY}^m) Y_X^X}{1 - \bar{A}_{XY}^Z}, \qquad (2.8)$$

where $\bar{A}_{XY}^m$ is the area fraction that the matrix pockets occupy in the $X-Y$ plane on the surface of the unit cell (it is equal to the ratio of the area of region A to the area $(1.81 + 1.25)^2$ mm^2 of the unit cell projected on the $X-Y$ plane). We assume all shear strengths to be equal ($Y_{ZX}^h = Y_{ZY}^h = Y_{XY}^h$) and given by a Voigt bound such that

$$Y_{ZX}^h = \frac{2v_X Y_{XY}^X + v_m \sigma_m/2}{2v_X + v_m}, \qquad (2.9)$$

where we have assumed that the matrix shear strength is $\sigma_m/2$ as per the Tresca yield criterion (we recognise that the Tresca criterion may not be completely appropriate for an epoxy resin, but used here in order simplify the analysis and get a first order estimate) . These plastic collapse and failure strengths are listed in Table 2.

Z-direction tow	$Y_Z^Z = 1300$	$Y_X^Z = Y_Y^Z = 170$	$Y_{XY}^Z = Y_{XZ}^Z = Y_{ZY}^Z = 85$
X-direction tow	$Y_X^X = 2800$	$Y_Z^X = Y_Y^X = 200$	$Y_{XY}^X = Y_{XZ}^X = Y_{ZY}^X = 100$
Homogenised matrix	$Y_Z^h = 1260$	$Y_X^h = Y_Y^h = 940$	$Y_{ZX}^h = Y_{ZY}^h = Y_{XY}^h = 92$

Table 2: The plastic/failure strengths of the tows and the homogenised matrix in the 3D noobed composite. In this table all the strengths are in MPa.

3. Measurements of the compressive response

The aim of the experimental study is to measure the compressive response of the 3D noobed composites and investigate the deformation/failure mechanisms. We first describe the measurement protocols and then proceed to discuss observations of the compressive behaviour.

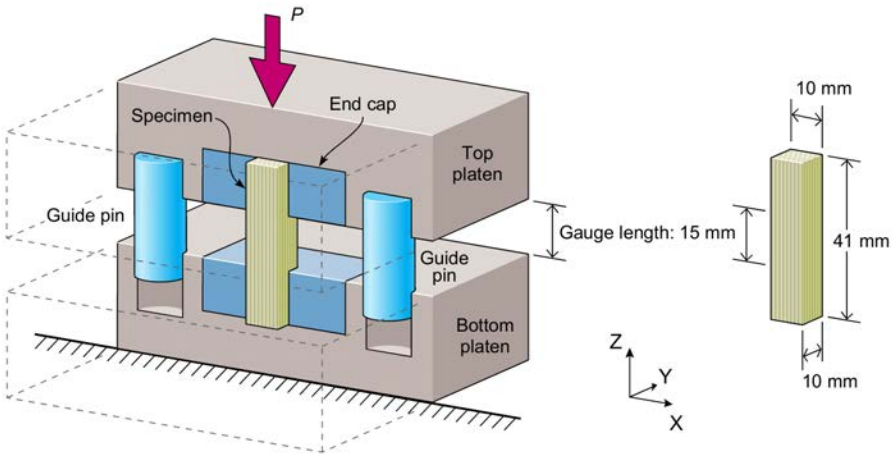

Figure 5: Sketch of the setup used for the compression of the 3D noobed composite in the Z and X-directions. The inset includes a sketch of the cuboidal specimen.

3.1 Measurement protocol

Tests were conducted to measure the response of these composites subjected to uniaxial compression in the Z-direction as well as the X and Y-directions. The

compressive response was measured using cuboidal specimens of length 41 mm and a 10 mm square cross-section, i.e. for compression in the Z-direction the 41 mm edge of the specimen was aligned with the Z-direction of the material while for compression in the X-direction the 41 mm edge was along the X-direction of the material. This size ensured that there were at least 3×3 Z-direction tows over the cross-section of the specimens used to measure the compressive responses in the Z-direction and the specimens used for measuring in the X-direction had 3×12 tows over the cross-section. The specimens were first cut to approximately the correct size using a diamond edged band-saw and then milled down to their final dimensions so as to ensure that the cuboids had parallel sides. These cuboids were then press-fitted into loading platens that had a 13 mm deep recess with a 10 mm cross section. This resulted in a compression setup wherein the gauge length of the specimen was 15 mm as sketched in Fig. 5. Guide-pins were employed as shown in Fig. 5 to minimize the introduction of bending loads into the specimen. Loading was performed in a screw-driven test machine at an applied cross-head displacement rate of 0.2 mm/min. The applied load was measured via the load cell of the test machine and used to define the nominal compressive stress σ_n while the compressive strain was measured via a laser extensometer over a 12 mm central gauge section of the specimen.

In addition to tests to measure the overall compressive response, we also performed interrupted tests wherein the specimens were unloaded after a specified level of compression and then imaged to observe the deformation/failure modes. Two types of imaging were performed: (i) XCT imaging which is non-destructive and (ii) high resolution optical imaging of the interior of the specimens. This optical imaging involved polishing of the specimen to expose the specimen interior and hence was a destructive process. The unloaded specimen was polished with SiC abrasive paper first using a coarse-grit (P220-P400) until approximately the mid-section of the specimen was exposed. Then, another 1 mm or so of the specimen was further abraded using a fine-grit (P800-P4000) in order to obtain a clean and smooth surface for imaging. In order to maximise the resolution of the images while still imaging a large enough area to clearly expose the deformation/failure modes, the imaged area was divided into a grid comprising approximately 200 squares. Each of these squares

was imaged separately and the entire imaged section was then reconstructed by stitching together these sub-images.

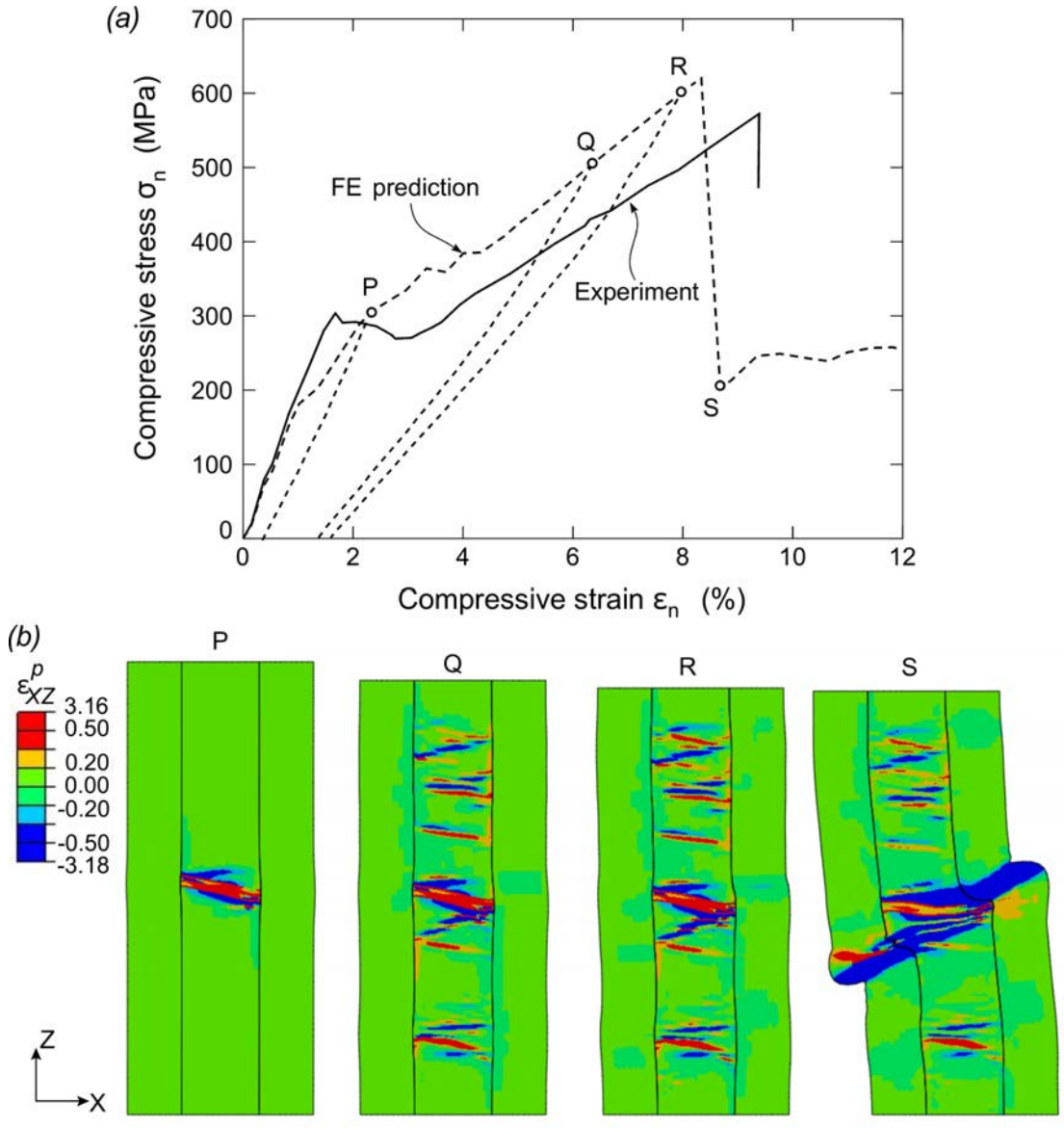

Figure 6: (a) The measured and FE prediction of the uniaxial compressive stress σ_n versus compressive strain ε_n response for compression in the Z-direction. FE predictions of the unloading response from selected applied strain levels prior to ultimate failure are also included. (b) FE predictions of the deformed unit cell with distributions of the plastic strain ε_{XZ}^{p} at four levels of applied strain (labelled P, Q, R and S) as indicated in (a). The images of the unit cell show the $X-Z$ plane.

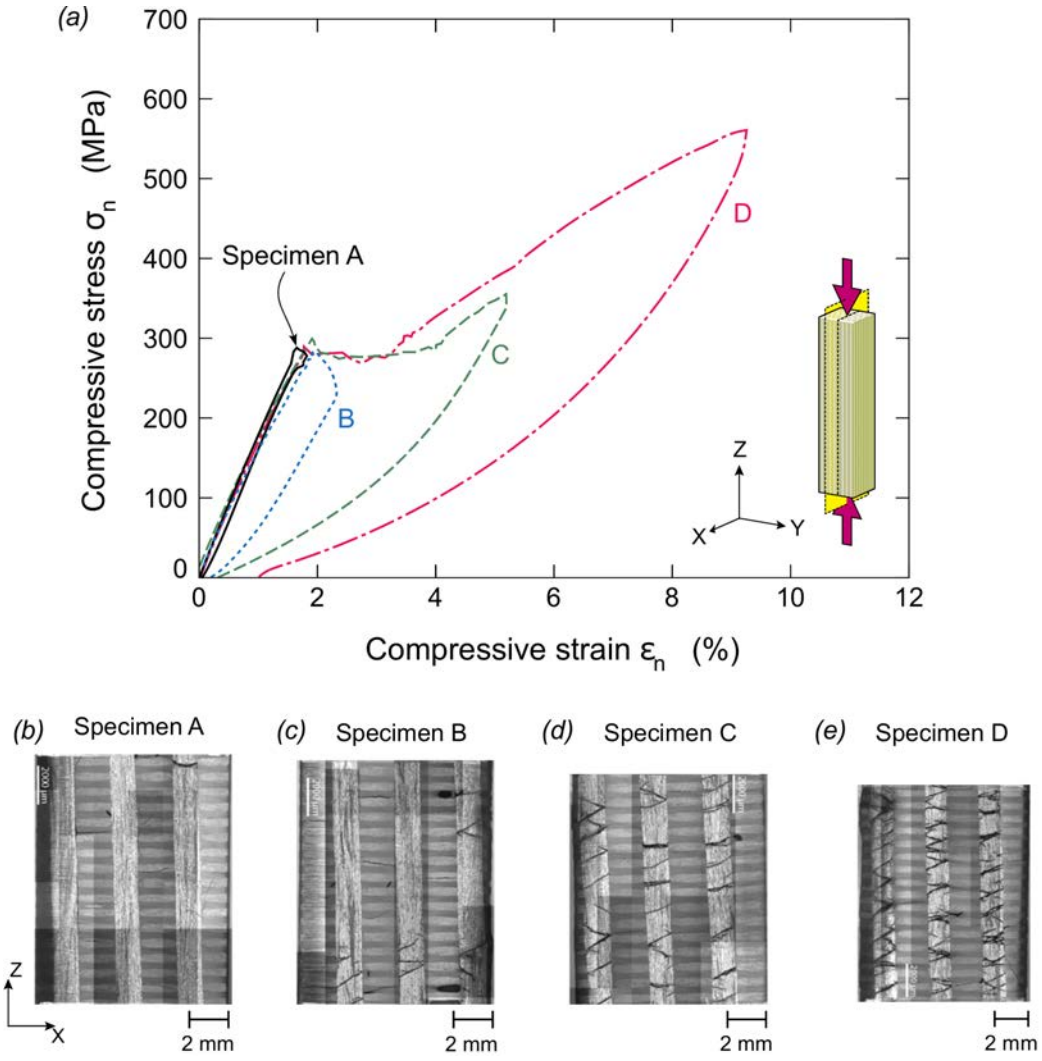

Figure 7: (a) Measured loading/unloading curves for compression in the Z-direction. The measurements are shown for four specimens (labelled A through D), each compressed to different levels of strain ε_n. The sketch in the inset shows plane along which the specimens were sectioned and optically imaged. (b-e) The development and propagation of kink-bands in the Z-direction tow in the 4 sectioned specimens.

3.2 Compression in the Z-direction

The measured uniaxial compression response in the Z-direction is plotted in Fig. 6a in terms of the applied nominal stress σ_n versus the nominal strain ε_n (here both the stress and strain are defined positive in compression). The measured response is atypical compared to the usual elastic-brittle compressive response of traditional CFRPs. In particular, after an initial elastic response with a modulus of 18.5 GPa, the 3D noobed composite displays a small stress plateau at around 300 MPa followed by almost linear strain hardening with a hardening modulus of 4.7 GPa. Fracture of the

specimen with loss of load carrying capacity occurs at a nominal compressive strain of about 10%, which is about a factor of three higher, compared to the compressive failure strains of usual CFRPs. In order to understand this rather unique compressive response we performed interrupted tests to visualise the deformation modes via optical microscopy as described above.

Tests on four different specimens (labelled A through D) were conducted with the tests interrupted after applied strains $\varepsilon_n = 1.8\%, 2.3\%, 5.3\%$ and 9.3%. The measured σ_n versus ε_n curves including the unloading responses are included in Fig. 7a for each of these specimens. Remarkably, the unloading behaviour is not linear elastic but upon load removal there is near complete recovery of the applied strain. This is reminiscent of reverse plasticity associated with the Bauschinger effect in metals. We proceed to discuss the reasons for this recovery along with the deformation mechanisms as discerned from the optical images.

The optical images of a section parallel to the $X - Z$ plane (see sketch in the inset of Fig. 7a) are included in Figs. 7b through 7e for the four specimens A through D, respectively. In each of the images, there are 3 tows in the Z-direction with the Y-direction tows and the matrix pockets giving rise to the banded microstructure between the Z-direction tows (the X-direction tows are not visible in the sectioned plane). In all the four samples there is no clear deformation visible in the Y-direction tows and the matrix pockets but there is clear evidence of the formation of bands of intense deformation, akin to kink bands in traditional unidirectional fibre composites, in the Z-direction tows. In specimen A, which was unloaded from $\varepsilon_n = 1.8\%$, a single kink is observed but with increasing applied strain ε_n the number of such kinks within the Z-direction tows increases and in fact some of these kinks "reflect" so that a zig-zag pattern of kinks is observed. We therefore infer that the non-linear deformation that commences at $\sigma_n \approx 300$MPa is due to the formation and propagation of these kink bands while the remainder to the composite (i.e. homogenised matrix) remains elastic. Thus, upon unloading there is the near complete recovery of the imposed strains as material surrounding the Z-direction tows recovers elastically.

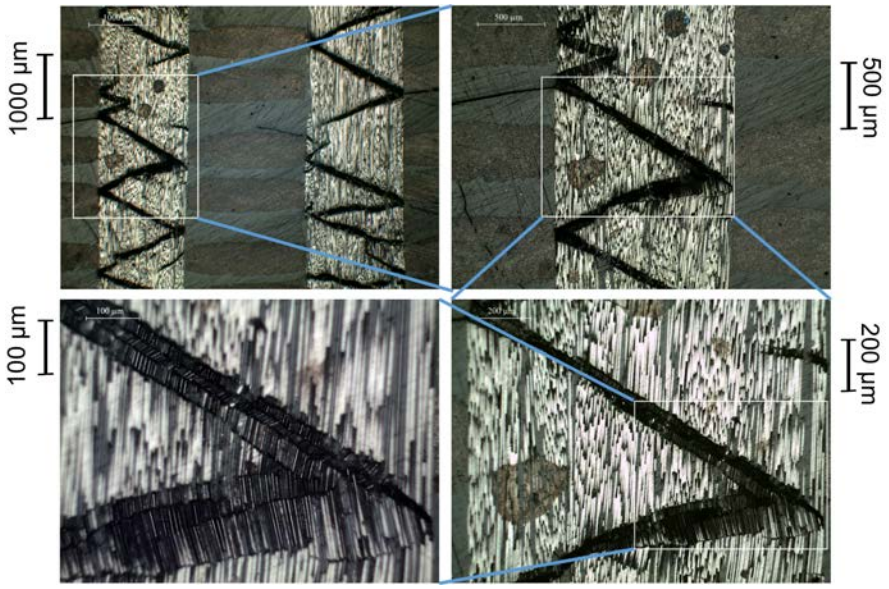

Figure 8: Optical micrographs of kinks in specimen D (Fig. 7a) at different levels of magnification.

While the dark bands in the Z-direction tows in Figs. 7b-7e are reminiscent of kinks it is instructive to observe the structure within these bands via higher resolution images. Such images are included in Fig. 8 (at four different levels of increasing magnification) for the kinks in specimen D. Clear evidence of fibre kinking with fibre fracture demarking the boundary between the kinked and unkinked regions is observed very similar to the well-established microbuckling/kinking behaviour in unidirectional carbon fibre composites. We proceed to discuss the differences and similarities between kinking in the Z-direction tows in these 3D composites and kinking in unidirectional CFRPs.

A magnified view of a kink-band in the Z-direction tow at an applied strain $\varepsilon_n = 2.3\%$ (just post the onset of the non-linearity in the stress versus strain response) is included in Fig. 9a. Budiansky (1983) estimated the kink width to be

$$\frac{w}{d} = \frac{\pi}{4}\left(\frac{E_Z^Z}{\tau_Y}\right)^{1/3} \qquad (3.1)$$

where from Section 2.3.1, $E_Z^Z = 65$ GPa is the longitudinal modulus of the Z-direction tow and $\tau_Y = 85$ MPa is the shear yield strength of Z-direction tow. The measured and predicted kink widths are in good agreement with $w = 51$ µm from Eq. (3.1) and the measured value of $w \approx 48$ µm. Next consider the stress σ_c for the

onset of non-linearity that is set by kink formation in the Z-direction tows. Since the homogenised matrix is elastic when micro-buckling is induced in the Z-direction tows it follows that σ_c is given by

$$\sigma_c = \bar{A}^Z_{XY}\sigma_b + (1 - \bar{A}^Z_{XY})\sigma_b \frac{E^h_Z}{E^Z_Z}, \qquad (3.2)$$

where $\bar{A}^Z_{XY} = 0.17$ is the area fraction of the Z-direction tows on the $X - Y$ plane while σ_b is the micro-buckling stress of the Z-direction tows. This micro-buckling stress is given in terms of the fibre-misalignment $\bar{\phi}$ with respect to the longitudinal axis as (Argon, 1972)

$$\sigma_b = \frac{\tau_Y}{\bar{\phi}}. \qquad (3.3)$$

Using the material parameters from Section 2.3 with $\bar{\phi} = 5^o$, we estimate $\sigma_c = 254$ MPa which is in reasonable agreement with the measurements. Thus, the onset of the non-linearity in the response including the width of the kink-band within the Z-direction tows is reasonably well predicted by the traditional kinking analysis. However, subsequent to the formation of the initial kink, the 3D noobed composite displays a hardening stress versus strain response (unlike traditional CFRPs). This is because the kinks in the Z-direction tows do not propagate into the rest of the composite but rather zig-zag as seen in Fig. 8. This is because the kinks are constrained by the material surrounding the Z-direction tows that remains elastic. However, in addition to the zig-zagging these kink bands also broaden as seen in micrograph at $\varepsilon_n \approx 9\%$ included in Fig. 9b: multiple fibre fractures and a kink width $w \approx 190\mu$m is observed in contrast to the $w \approx 48\mu$m kink band in Fig. 9a where a single line of fibre fracture demarcates the kink boundary. We thus conclude that while there are clear similarities with the compressive response of traditional CFRPs, the 3D noobed composites differ by: (i) displaying a hardening compressive response with a large compressive ductility and (ii) the formation of multiple kinks (some of which zig-zag) rather than a single kink band.

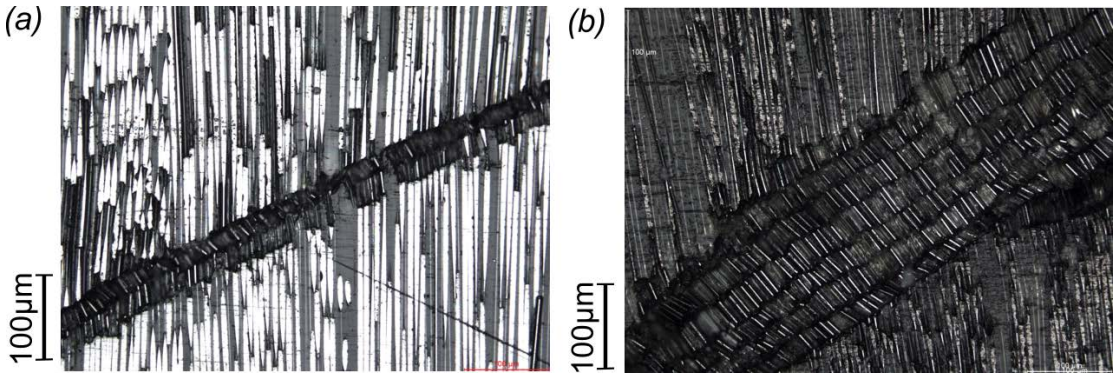

Figure 9: Optical micrographs that show kink-bands in the Z-direction tow for a specimen compressed in the Z-direction to strains (a) $\varepsilon_n \approx 2\%$ and (b) $\varepsilon_n \approx 9\%$.

3.3 Compression in the X or Y – directions

The compressive response of the 3D noobed composite in the X and Y-directions is indistinguishable and hence here we only discuss the compressive behaviour in the X-direction. The measured response is included in Fig. 10a and the key differences with respect to the compression response in the Z-direction are: (i) a higher modulus in the X-direction; (ii) a higher critical stress for the onset of the non-linearity and (iii) no hardening subsequent to the onset of the non-linearity with a significantly lower ductility compared to compression in the Z-direction. These differences can be understood in terms of the high fibre volume fractions in the X and Y-direction tows compared to the Z-direction tows. We proceed here to explain these differences in a qualitative manner with a detailed numerical analysis given in Section 4.

The higher modulus of the 3D noobed composite in the X-direction follows directly from the fact that the X-direction tows have a higher fibre volume fraction with $f_X \approx 68\%$ and that the volume fraction of the X-direction tows $v_X > v_Z$. In order to understand the compressive failure mechanisms and lower compressive ductility we performed both interrupted tests with XCT scans of the specimen and destructive optical imaging. The XCT scans (after unloading) of the specimens at three different stages of the deformation are included in Fig. 11. Scan A is in the elastic domain and there is no clear visible deformation/failure in the images of the $X-Z$ and $X-Y$ planes. Some evidence of cracking is visible in scan B which is taken immediately after the peak load is attained while scan C which is taken after loading to $\varepsilon_n \approx 3.5\%$ shows extensive localisation of the deformation across the entire specimen width.

However, the resolution of these XCT scans is not sufficient to discern the fibre fracture modes and hence we also performed destructive optical imaging of a specimen deformed to just beyond the peak load. These optical images are included in Fig. 12 showing views of two different planes $X-Z$ and $X-Y$. Intriguingly, similar to the multiple kink bands seen in the Z-direction tows in Figs. 7 and 8, multiple and zig-zagged kinks are also observed in the X-direction tows although this multiple kinking is not as extensive. We thus hypothesize that the formation of these kinks sets the peak compressive stress. However, unlike compression in the Z-direction there is no hardening beyond the stress required to initiate kinking. We attribute this to the high strength in the X-direction and the relatively low shear strength of the Z-directions tows that allows kinks that form in the X-direction tows to propagate across the specimen width. We shall use FE calculations to better understand this deformation mode and the differences between the compressive responses in the X and Z-directions.

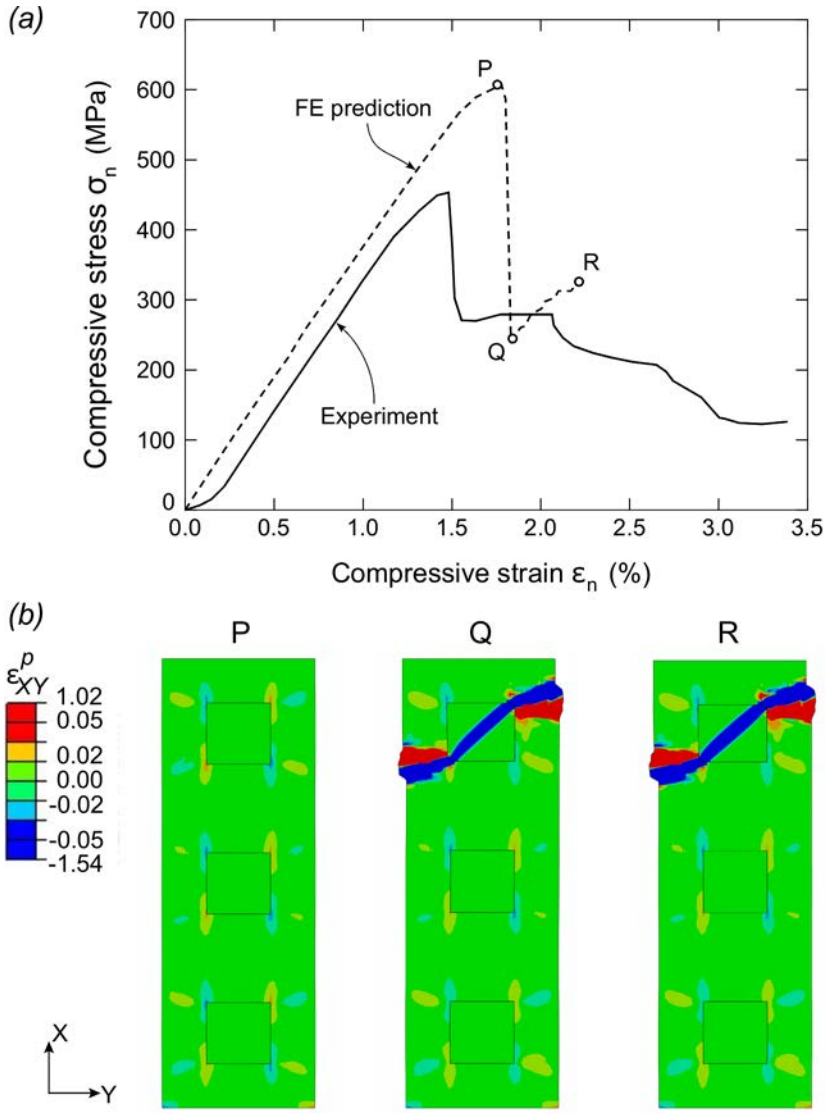

Figure 10: (a) The measured and FE prediction of the uniaxial compressive stress σ_n versus compressive strain ε_n response for compression in the X-direction. (b) FE predictions of the deformed unit cell with distributions of the plastic strain ε_{XY}^{p} at three levels of applied strain (labelled P, Q and R) as indicated in (a). The images of the unit cell show the $X-Y$ plane.

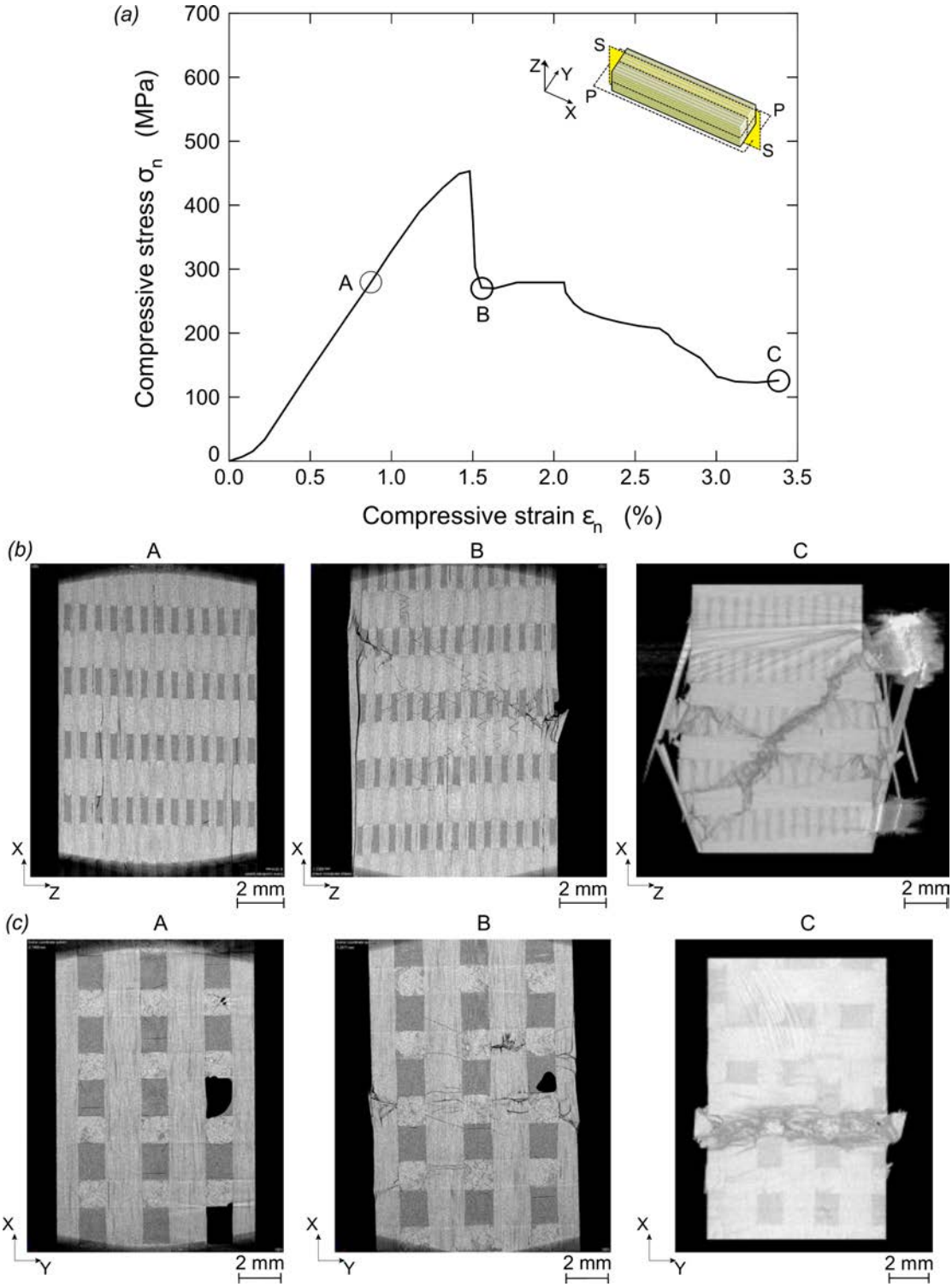

Figure 11: XCT scans of the 3D noobed composite at three levels of compression in the X-direction. (a) The measured stress σ_n versus strain ε_n response with the strain levels (labelled A through C) where the specimen was imaged marked. The inset shows a sketch of the imaged planes. XCT images of the three specimens with views of the (b) $X-Z$ plane and (c) the $X-Y$ plane.

4. Finite element modelling of the compressive response

In order to improve our understanding of the observed deformation and failure modes we report FE calculations of the compressive responses in the Z and X-directions. These calculations are continuum calculations wherein the discrete microstructure comprising fibres and matrix is not modelled explicitly. Rather, we keep the model relatively simple so as to aid interpretation but of course include sufficient physics to capture the experimental observations. With this in mind we report calculations where the composite is modelled using the homogenised properties of the tows as reported in Section 2.3.

We analyse two separate repeating unit cells for compression in the X and Z-directions. The unit cell for the analysis of the compression in the Z-direction is first described. The repeating unit cell is cuboidal with a square cross-section of side 3.06 mm and height 7.5 mm representing half the gauge length of the tested specimen. The cell comprises a single Z-direction tow of cross-section $1.25\ \text{mm} \times 1.25\ \text{mm}$ surrounded by the X and Y-direction tows as well as the matrix pockets as shown in Fig. 13a. While the Z-direction tow is modelled as a distinct material with properties as described in Section 2.3, the X and Y-direction tows as well as the matrix pockets are not modelled explicitly but rather as a single homogenous continuum (Fig. 13b), i.e. as the homogenised matrix described in Section 2.3. This approximation is employed as the very large number of distinct constituents that are present in the material surrounding the Z-direction tow makes the fully discrete approach numerically very expensive. The unit cell for modelling compression in the X-direction is sketched in Fig. 13c. This cell is also a cuboid with a rectangular cross-section of sides 3.06 mm (Y) and 2.4 mm (Z) and height 9.18 mm. Thus, the unit cell comprises three Z-direction tows as shown in Fig. 13c surrounded by the homogenised matrix consistent with the approach used to the model the Z-direction compression.

4.1 Material model

Two anisotropic materials are used to model the Z-direction tows and the homogenised matrix. Here we detail the material properties used to describe both these materials. A tow comprising a high volume fraction of nearly rigid fibres in a

polymer matrix is likely to be best described by an anisotropic frictional model with non-associated flow. Some attempts in this direction have been made; see for example Vogler et al. (2013). However, such models require additional parameters including the friction angle that are not available for the noobed composite and hence here we use a simplified treatment. Specifically, both materials are modelled as anisotropic elastic, perfectly plastic materials with the anisotropic plasticity described by the Hill (1948) anisotropic plasticity model.

First consider the Z-direction tow. We model it as a transversely isotropic medium with the Z or fibre direction being normal to the plane of isotropy. Then the elastic strains ε_{ij}^{e} are related to the stresses σ_{ij} in the (X, Y, Z) co-ordinate system via 5 independent elastic constants as

$$\begin{pmatrix} \varepsilon_{XX}^{e} \\ \varepsilon_{YY}^{e} \\ \varepsilon_{ZZ}^{e} \\ \varepsilon_{YZ}^{e} \\ \varepsilon_{XZ}^{e} \\ \varepsilon_{XY}^{e} \end{pmatrix} = \begin{pmatrix} 1/E_X^Z & -\nu_{YX}^Z/E_X^Z & -\nu_{ZX}^Z/E_Z^Z & 0 & 0 & 0 \\ -\nu_{XY}/E_X^Z & 1/E_X^Z & -\nu_{ZX}^Z/E_Z^Z & 0 & 0 & 0 \\ -\nu_{XZ}^Z/E_X^Z & -\nu_{XZ}^Z/E_X^Z & 1/E_Z^Z & 0 & 0 & 0 \\ 0 & 0 & 0 & 1/(2G_{YZ}^Z) & 0 & 0 \\ 0 & 0 & 0 & 0 & 1/(2G_{YZ}^Z) & 0 \\ 0 & 0 & 0 & 0 & 0 & (1+\nu_{XY}^Z)/E_X^Z \end{pmatrix} \begin{pmatrix} \sigma_{XX} \\ \sigma_{YY} \\ \sigma_{ZZ} \\ \sigma_{YZ} \\ \sigma_{XZ} \\ \sigma_{XY} \end{pmatrix}. \quad (4.1)$$

The total strain rate is then written as the sum of the elastic and plastic strain rates such that

$$\dot{\varepsilon}_{ij} = \dot{\varepsilon}_{ij}^{e} + \dot{\varepsilon}_{ij}^{p}, \quad (4.2)$$

with the plastic strain rate given by the associated flow rule

$$\dot{\varepsilon}_{ij}^{p} = \dot{\lambda}\frac{\partial \Phi}{\partial \sigma_{ij}}, \quad (4.3)$$

in terms of the plastic multiplier $\dot{\lambda}$ and the Hill yield potential Φ. This potential is specified in terms of the constants F, G, H, L, M and N as

$$\begin{aligned} 2\Phi \equiv F(\sigma_{YY}-\sigma_{ZZ})^2 + G(\sigma_{ZZ}-\sigma_{XX})^2 + H(\sigma_{XX}-\sigma_{YY})^2 \\ + 2L\sigma_{YZ}^2 + 2M\sigma_{ZX}^2 + 2N\sigma_{XY}^2, \end{aligned} \quad (4.4)$$

such that continued plastic flow occurs with $\Phi = 1/2$. The six constants F, G, H, L, M and N then follow from six strengths with respect to the principal axes of anisotropy, i.e.

$$G+H=\frac{1}{(Y_X^Z)^2},\quad F+H=\frac{1}{(Y_Y^Z)^2}\quad\text{and}\quad G+F=\frac{1}{(Y_Z^Z)^2},\qquad(4.5)$$

where Y_X^Z, Y_Y^Z and Y_Z^Z are the tensile strengths in the X, Y and Z-directions, respectively (note that the Hill model assumes equal compressive and tensile strengths). Similarly, the shear strengths Y_{YZ}^Z, Y_{ZX}^Z and Y_{XY}^Z give the remaining constants via

$$L=\frac{1}{2(Y_{YZ}^Z)^2},\quad M=\frac{1}{2(Y_{ZX}^Z)^2}\quad\text{and}\quad N=\frac{1}{2(Y_{XY}^Z)^2}.\qquad(4.6)$$

The 5 elastic constants and the 6 strengths required for the constitutive model of the Z-direction tow are listed in Tables 1 and 2, respectively.

The material surrounding the Z-direction tows comprises the X and Y-direction tows as well as the matrix pockets. This material is modelled as a single effective medium labelled the "homogenised matrix". Based on the discussion in Section 2.3, we model this homogenised matrix as a transversely isotropic medium with the Z-direction being normal to the plane of isotropy. Thus, again we use an elastic law of the form Eq. (4.1) with plastic flow modelled via Hill's anisotropic plastic model. The elastic and plastic properties of this effective medium as derived in Section 2.3 are listed in Tables 1 and 2, respectively. These properties can be used in the elastic law that is analogous to Eq. (4.1) and also to determine the 6 constants of the Hill model.

4.2 The boundary value problem

The finite element (FE) calculations were performed using the commercial FE package ABAQUS with the unit cells (Figs. 13b and 13c) discretised using 8 noded linear brick elements with reduced integration (C3D8R in the ABAQUS notation). Cubic elements of side approximately 0.05 mm were employed to discretise both the Z-direction tows and the surrounding homogenised matrix: calculations with further mesh refinements revealed no significant changes in the numerical results. Uniaxial compression was simulated by enforcing displacement boundary conditions on the top and bottom surfaces of the unit cell with the four side surfaces being traction-free: periodic boundary conditions were not enforced so as to allow the formation of kink-bands. Since the unit cell had 1/9th the cross-sectional area of the specimen employed in the experiments, we needed to ensure that global buckling was not operative in the numerical simulations. We achieved this by analysing a unit cell with about half the

gauge height of the specimen used in the experiments. In all the calculations perfect bonding was assumed between the Z-direction tow and the surrounding homogenised matrix.

In the Z-direction compression calculations, an imperfection was introduced into the Z-direction tow in order to initiate a kink band. This imperfection as sketched in Fig. 13d comprised a region of width $w = 200$ μm inclined at an angle $\beta = 20^{o}$ with respect to the X-direction. The fibres were assumed to be misaligned within this imperfect region. This misalignment was specified by rotating the principal axes of the material anisotropy such that the material Z-direction was at an angle $\bar{\phi} = 5^{o}$ with respect to the global Z-direction in the $X - Z$ plane as shown in Fig. 13d. Such a prescription of the initial imperfection to initiate a kink-band is commonly employed (Kyriakides et al., 1995; Kyriakides and Ruff, 1997) and consistent with a range of experimental observations (Moran et al., 1995). No imperfection was employed for the X-direction compression simulations as the X-direction tows were not explicitly modelled but rather homogenised with the Y-direction tows and the matrix pockets.

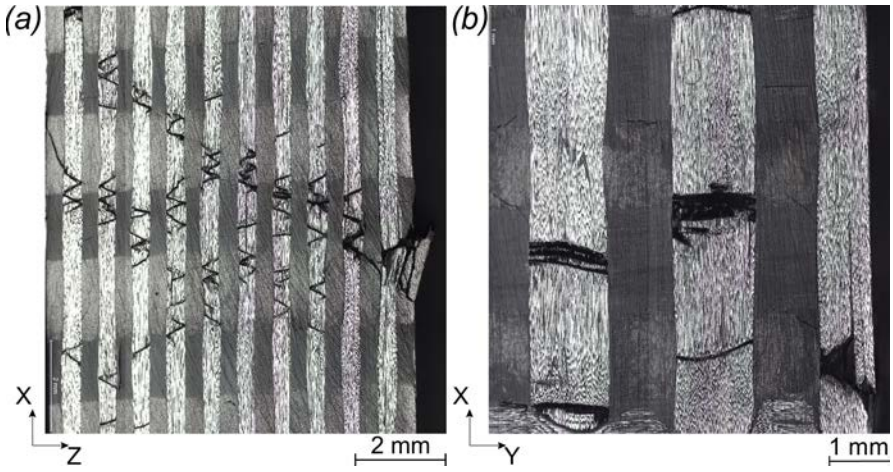

Figure 12: Optical micrographs of the 3D noobed composite compressed in the X-direction to just beyond the peak load. The images are taken on central sections through the specimen on (a) the $X - Z$ plane and (b) the $X - Y$ plane.

4.3 Numerical results

The FE prediction of the Z-direction compressive response of the composite is included in Fig. 6a while predictions of the deformed configurations of the unit cell at

four selected values of applied strain ε_n are included in Fig. 6b (marked P, Q, R and S in Fig. 6a). Contours of the plastic strain ε_{XZ}^p are included in these images to highlight the regions of the local deformations and the associated kink-bands. The FE prediction of the overall stress versus strain response is in excellent agreement with the measurements (Fig. 6a). This agreement follows from predictions of the deformation modes seen in Fig. 6b. At around the onset of non-linearity (P) a kink-band forms in the Z-direction tow from the initial imperfection included in the tow. With increasing strain (Q) there is negligible plastic straining outside the Z-direction tow but multiple kinks including reflected kinks are observed in the Z-direction tow in line with the micrographs in Fig. 7. At near the peak stress (R), plastic deformation is seen to initiate in the material outside the Z-direction tow and beyond the peak load (S) a kink band that spans across the entire width of the unit cell is predicted consistent with the overall failure of the specimen. These results demonstrate that the onset of the non-linearity is set by kink band formation and hence accurately predicted by Eqs. (3.2) and (3.3). On the other hand, the subsequent hardening is mainly due to the elastic compression of the material surrounding the Z-direction tow. Consequently, consistent with the measurements shown in Fig. 7a, the unloading FE calculations predict significant recovery of the applied compressive strains along with reverse plasticity in the Z-direction tows. Final failure results from failure of the surrounding material via the indirect tension mechanism discussed in Section 2.3. This understanding allows an approximate estimation of the peak strength by assuming that the Z-direction tow has no load carrying capacity after the onset of kinking. The peak strength σ_p is then given as $\sigma_p = (1 - \bar{A}_{XY}^Z)Y_Z^h \approx 1$ GPa where $Y_Z^h = 1260$ MPa(Table 2). This approximate prediction overestimates the strength even though it ignores any contribution from the Z-direction tow. We trace this discrepancy to the fact that this approximate analysis neglects the stress concentrations that develop in the homogenised matrix due to the formation of kinks in the Z-direction tow. Hence, full FE calculations as performed here are required to accurately predict these stress concentrations and the peak Z-direction strength of the composite. We emphasize here that consistent with the measurements, the FE calculations predict elastic recovery of the specimen prior to collapse of the entire specimen. This is because even though the Z-direction tow forms kinks and deforms plastically, the surrounding material remains elastic.

Prediction of the X-direction compressive response is included in Fig. 10a with deformed configurations shown in Fig. 10b at selected applied strains (marked P, Q and R in Fig. 10a). Here contours of the plastic strain ε_{XY}^{p} are included on the deformed configurations. The FE prediction of the stress versus strain response is in reasonable agreement with the measurements except for the fact that the FE calculations over-predict the peak strength. This is because no initial imperfection is included in these FE calculations since the X-direction tows are not explicitly modelled. Consistent with observations (Figs. 11 and 12) no significant localised deformation is observed prior to the peak stress though the FE calculations show strain concentrations emanating from the corners of the Z-direction tows. At the peak stress, kink bands initiated from these concentrations at the corners of the Z-direction tows span across the unit cell. Consistent with the measurements, these kink bands cause a large loss in load carrying capacity. We emphasize here that since the X-direction tows are not explicitly modelled, this model does not have the resolution required to study the formation of kink bands within these tows as seen in Fig. 12. Thus, formation of kink-bands in the effective material around the Z-direction tows results in complete collapse of the specimen. This is because the Z-direction tows are weaker compared to the X and Y-direction tows (as they have a smaller fibre volume fraction) and have already attained their transverse collapse stress prior to the failure of the homogenised matrix. In summary, we hypothesise that high compressive ductility is only expected when the material surrounding the tows in the compression direction has a higher compressive strength than the tows undergoing axial compression. Of course, further experiments in which fibre volume fractions in the noobed composites are varied and associated FE calculations are required to confirm this hypothesis. This is beyond the scope of the current investigation.

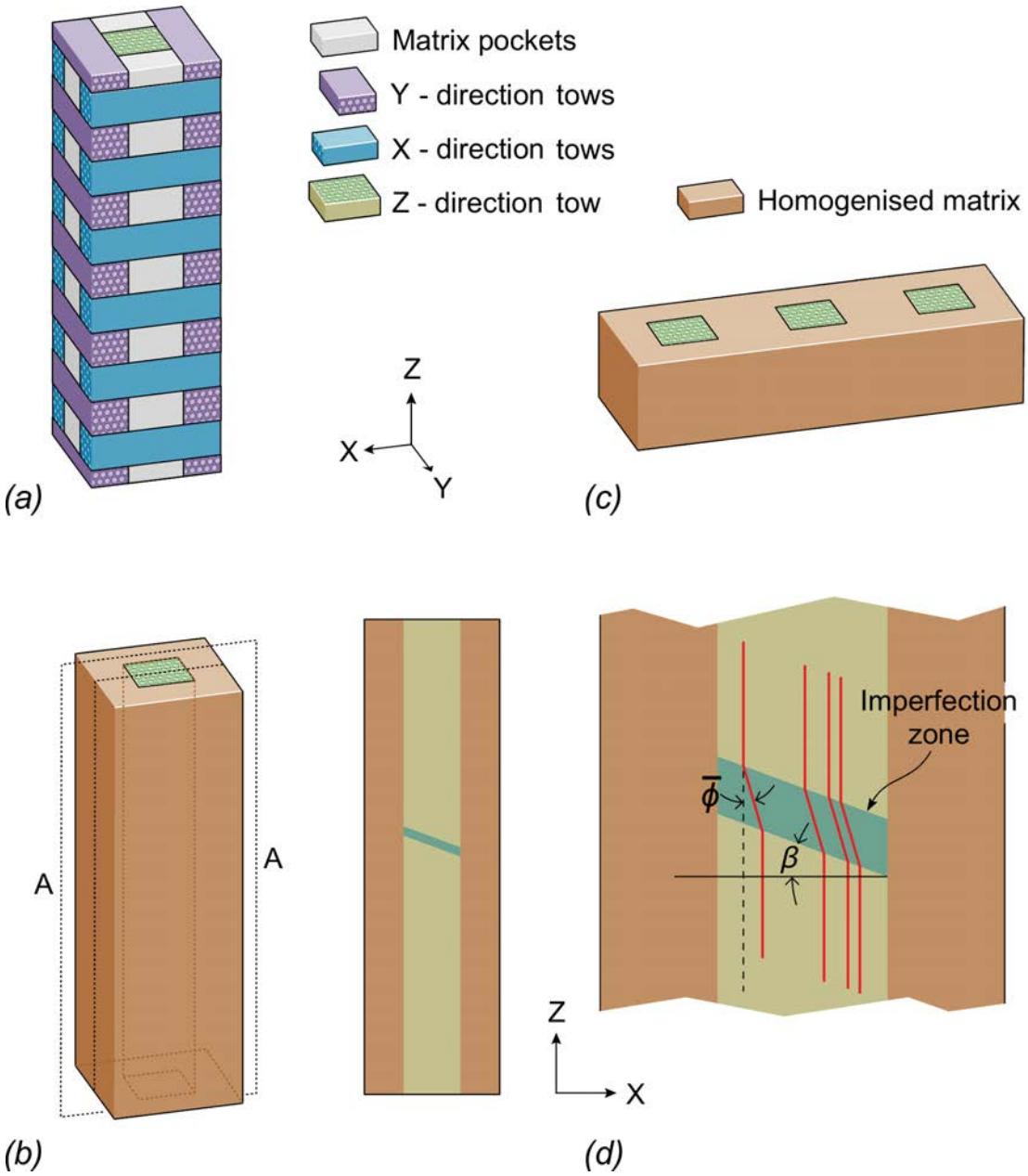

Figure 13: (a) Sketch of the unit cell of the 3D noobed composite for compression in the Z-direction. The sketch shows four separate constituent phases of the composite within the unit cell. Sketches of the unit cell with the homogenised matrix used in the FE calculations of compression in the (b) Z-direction and (c) X-direction. (d) A sketch of section AA of the unit cell in (b) to illustrate the geometric imperfection included in the Z-direction tow.

5. Concluding remarks

We have reported the compressive response of a carbon fibre/epoxy composite comprising non-interlaced carbon fibre tows in three orthogonal directions produced

by the noobing process. In contrast to traditional unidirectional and two-dimensional (2D) composites, stable and multiple kinks form in the tows aligned with the compression direction. This is due to the constraint imposed by the surrounding material that comprises tows in two orthogonal directions. Compression in the low fibre volume fraction direction results in a high compressive ductility of about 10%. The onset of the nonlinear response occurs at about 2% applied strain associated with the formation of kink bands within the tows in the compression direction. These initial kink bands are well predicted by the well-established micro-buckling theories developed for unidirectional fibre composites. However, unlike traditional CFRPs these noobed 3D composites display a subsequent stable and strain hardening response along with the formation of multiple zig-zagging kink bands. Finite element (FE) calculations with the tows modelled as anisotropic continua are also reported to understand the deformation/failure modes in these composites. These FE calculations predict both the compressive response and the observed deformation and failure modes including the zig-zagging kink bands with reasonable accuracy. In particular, the FE calculations confirm that for compression in the low fibre volume fraction direction, overall failure of the composites is not set by the formation of kink bands within the tows aligned with the compression direction. Rather the loss of load carrying capacity results from compressive failure of the material surrounding tows aligned with the compression direction.

Acknowledgements

The authors are grateful to the Office of Naval Research (ONR) for their financial support through grant number N62909-16-1-2127 on Dynamic performance of 3D assembled composite structures (program managers Dr Joong Kim & Dr Judah Goldwasser).

References

Argon, A.S., 1972. Fracture of composites. In *Treatise on materials science and technology,* Vol I., 79–114.

Attwood, J.P., Khaderi, S.N., Karthikeyan, K., Fleck, N.A., Masta, M.R.O., Wadley, H.N.G., Deshpande, V.S., 2014. The out-of-plane compressive response of Dyneema composites. *J. Mech. Phys. Solids* **70**, 200–226.

Bele, E., Deshpande, V.S., 2015. The compressive response of idealized Cermet-like materials. *J. Appl. Mech.* **82**, 1–11. doi:10.1115/1.4029782

Budiansky, B., 1983. Micromechanics. *Comput. Struct.* **16**, 3–12. doi:10.1016/0045-7949(83)90141-4

Fleck, N.A., 1997. Compressive failure of fiber composites. *Adv. Appl. Mech.* **33**, 43-117.

Freitas, G., Magee, C., Dardzinski, P., Fusco, T., 1994. Fiber insertion process for improved damage tolerance in aircraft laminates. *J. Adv. Mater.* **25**, 36–43.

George, T., Deshpande, V.S., Wadley, H.N.G., 2014. Hybrid carbon fiber composite lattice truss structures. *Compos A, Appl. Sci. Manuf.* **65**, 135–147.

Hashin, Z., 1962. The elastic moduli of heterogeneous materials. *ASME J. Appl. Mech.* **29**, 143–150.

Hill, R., 1948. A theory of the yielding and plastic flow of aniosotropic metals. *Proceedings of the Royal Society of London A* **193**, 281– 297.

Kamiya, R., Cheeseman, B.A., Popper, P., Chou, T.W., 2000. Some recent advances in the fabrication and design of three-dimensional textile preforms: A review. *Compos. Sci. Technol.* **60**, 33–47. doi:10.1016/S0266-3538(99)00093-7

Khokar, N., 2002. Noobing: A nonwoven 3D fabric-forming process explained. *J. Text. Inst.* **93**, 52–74. doi:10.1080/00405000208630552

Khokar, N., 1996. 3D fabric-forming processes: distinguishing between 2D-weaving, 3D-weaving and an unspecified non-interlacing process. *J. Text. Inst.* **87**, 97–106. doi:10.1080/00405009608659059

Khokar, N., 2012. A 3D fabric and a method and apparatus for producing such a 3D fabric. PCT/EP2012/055240.

Kuo, W.S., Ko, T.H., 2000. Compressive damage in 3-axis orthogonal fabric composites. *Compos. A, Appl. Sci. Manuf.* **31**, 1091–1105. doi:10.1016/S1359-835X(00)00066-X

Kuo, W.S., Ko, T.H., Chen, C.P., 2007. Effect of weaving processes on compressive behavior of 3D woven composites. *Compos. A, Appl. Sci. Manuf.* **38**, 555–565. doi:10.1016/j.compositesa.2006.02.025

Kyriakides, S., Arseculeratne, R., Perry, E.J., Liechti, K.M., 1995. On the compressive failure of fiber reinforced composites. *Int. J. Solids Struct.* **32**, 689–738. doi:10.1016/0020-7683(94)00157-R

Kyriakides, S., Ruff, A.E., 1997. Aspects of the failure and postfailure of fiber composites in compression. *J. Compos. Mater.* **31**.

Laffan, M.J., Pinho, S.T., Robinson, P., Iannucci, L., McMillan, A.J., 2012. Measurement of the fracture toughness associated with the longitudinal fibre compressive failure mode of laminated composites. *Compos. A, Appl. Sci. Manuf.* **43**, 1930–1938. doi:10.1016/j.compositesa.2012.04.009

Malcom, A. J., Aronson, M.T., Deshpande, V.S., Wadley, H.N.G., 2013. Compressive response of glass fiber composite sandwich structures. *Compos. A, Appl. Sci. Manuf.* **54**, 88–97. doi:10.1016/j.compositesa.2013.07.007

McIlhagger, R., Quinn, J.P., McIlhagger, A.T., Wilson, S., Simpson, D., Wenger, W., 2008. The influence of binder tow density on the mechanical properties of spatially reinforced composites. Part 2 - Mechanical properties. *Compos. A, Appl. Sci. Manuf.* **39**, 334–341.

McIlhagger, R., Quinn, J.P., McIlhagger, A.T., Wilson, S., Simpson, D., Wenger, W., 2007. The influence of binder tow density on the mechanical properties of spatially reinforced composites. Part 1 – Impact resistance. *Compos. A, Appl. Sci. Manuf.* **38**, 795–801.

Moran, P.M., Liu, X.H., Shih, C.F., 1995. Kink band formation and band broadening in fiber composites under compressive loading. *Acta Metall. Mater.* **43**, 2943–2958. doi:10.1016/0956-7151(95)00001-C

Mouritz, A.P., 2007. Review of z-pinned composite laminates. *Compos. A, Appl. Sci. Manuf.* **38**, 2383–2397. doi:10.1016/j.compositesa.2007.08.016

Pinho, S.T., Darvizeh, R., Robinson, P., Schuecker, C., Camanho, P., 2012. Material and structural response of polymer-matrix fibre-reinforced composites. *J. Compos. Mater.* **46**, 2313–2341. doi:10.1177/0021998312454478

Poe, C.C., Dexter, H.B., Raju, I.S., 1999. A review of the NASA textile composites research. *J. Aircr.* **36**(5), 876-884.

Quinn, J.P., McIlhagger, A.T., McIlhagger, R., 2008. Examination of the failure of 3D woven composites. *Compos. A, Appl. Sci. Manuf.* **39**, 273–283. doi:10.1016/j.compositesa.2007.10.012

Sivashanker, S., Fleck, N.A., Sutcliffe, M.P.F., 1996. Microbuckle propagation in a unidirectional carbon fibre-epoxy matrix composite. *Acta Mater*. **44**, 2581–2590. doi:10.1016/1359-6454(95)00410-6

Stig, F., 2012. 3D-woven reinforcement in composites [Doctoral thesis]. KTH Royal Institute of Technology.

Suquet, P.M., 1993. Overall potentials and extremal surfaces of power law or ideally plastic composites. *J. Mech. Phys. Solids* **41**, 981–1002.

Tan, P., Tong, L., Steven, G.P., Ishikawa, T., 2000. Behavior of 3D orthogonal woven CFRP composites. Part I. Experimental investigation. *Compos. A, Appl. Sci. Manuf*. **31**, 259–271.

Vogler, T.J., Kyriakides, S., 1997. Initiation and axial propagation of kink bands in fiber composites. *Acta Mater*. **45**, 2443–2454. doi:10.1016/S1359-6454(96)00350-3

Vogler, M., Rolfes, R., Camanho, P.P., 2013. Modeling the inelastic deformation and fracture of polymer composites — Part I: Plasticity model. *Mech. Mater*. **59**, 50– 64.

Wind, J.L., Waas, A.M., Jensen, H.M., 2015. Initiation of failure at notches in unidirectional fiber composites. *Compos. Struct*. **122**, 51–56. doi:10.1016/j.compstruct.2014.11.043